



This is a repository copy of *Influence of powder-bed temperature on the microstructure and mechanical properties of Ti-6Al-4V produced by selective laser melting*.

White Rose Research Online URL for this paper:  
<http://eprints.whiterose.ac.uk/162376/>

Version: Submitted Version

---

**Article:**

Pedrazzini, S., Pek, M.E., Ackerman, A.K. et al. (10 more authors) (Submitted: 2020)  
Influence of powder-bed temperature on the microstructure and mechanical properties of Ti-6Al-4V produced by selective laser melting. arXiv. (Submitted)

---

© 2020 The Author(s). For reuse permissions, please contact the Author(s).

**Reuse**

Items deposited in White Rose Research Online are protected by copyright, with all rights reserved unless indicated otherwise. They may be downloaded and/or printed for private study, or other acts as permitted by national copyright laws. The publisher or other rights holders may allow further reproduction and re-use of the full text version. This is indicated by the licence information on the White Rose Research Online record for the item.

**Takedown**

If you consider content in White Rose Research Online to be in breach of UK law, please notify us by emailing [eprints@whiterose.ac.uk](mailto:eprints@whiterose.ac.uk) including the URL of the record and the reason for the withdrawal request.



[eprints@whiterose.ac.uk](mailto:eprints@whiterose.ac.uk)  
<https://eprints.whiterose.ac.uk/>

# Influence of powder-bed temperature on the microstructure and mechanical properties of Ti-6Al-4V produced by selective laser melting

S. Pedrazzini<sup>1\*</sup>, M. E. Pek<sup>1\*</sup>, A. K. Ackerman<sup>1</sup>, H. Ali<sup>2,3</sup>, H. Ghadbeigi<sup>2</sup>, K. Mumtaz<sup>2</sup>, T. Dessolier<sup>1</sup>, T.B. Britton<sup>1</sup>, P. Bajaj<sup>4</sup>, E. Jäggle<sup>4</sup>, B. Gault<sup>1,4</sup>, A. J. London<sup>5</sup>, E. Galindo-Nava<sup>6</sup>

<sup>1</sup> Department of Materials, Imperial College London, South Kensington Campus, Exhibition Road, SW7 2AG, London, UK.

<sup>2</sup> Department of Mechanical Engineering, University of Sheffield, Western Bank, Sheffield, S1 3JD, UK.

<sup>3</sup> University of Engineering & Technology, Jamrud Road, Peshwar Khyber Pakhtunkhwa, Pakistan.

<sup>4</sup> Max-Planck Institute für Eisenforschung, Max-Planck Straße 1, 40237, Düsseldorf, Germany.

<sup>5</sup> UK Atomic Energy Authority, Culham Science Centre Abingdon OX14 3EB, UK.

<sup>6</sup> Department of Materials Science and Metallurgy, University of Cambridge, 27 Charles Babbage Road, CB3 0FS, Cambridge, UK.

\*These two authors contributed equally.

## Abstract

Additive manufacturing's capacity to produce near-net shaped complex geometries has generated interest across many industries. However, the mechanical properties of Ti-6Al-4V produced by Laser Powder Bed Fusion (LPBF) are not comparable yet to samples produced through conventional manufacturing methods. In the present work, advanced characterisation techniques were used on LPBF Ti-6Al-4V samples produced on a heated base plate to study the complex variations in microstructure and solute behaviour associated to changes in strength and ductility at different preheating temperatures. When the substrate temperature is 100 °C the elongation is ~6%, which increases and peaks at ~10% at 570 °C, then sharply decreases to zero ductility at 770 °C. The ultimate strength at 100°C and 570°C remains high and approximately constant (~1.2GPa) and it has the lowest value at 770°C, due to the alloy's brittle behaviour. At 100°C, a heavily strained and twinned microstructure, primarily composed of  $\alpha+\alpha'$ , was observed and it was comparable to as-built microstructures obtained by conventional LPBF methods. At higher temperatures, twins are no longer present and instead nano-scale  $\beta$  precipitates are observed within  $\alpha'$  and  $\alpha$ , as well as dislocation networks (570°C) and tangles (770°C). The lack of twins was attributed to the preheating temperatures being above the twin recovery temperature and the presence of the dislocation networks and tangles was attributed to interfacial dislocations forming at the  $\alpha'/\beta$  interface, as  $\alpha'$  forms upon rapid cooling. Solute segregation at crystal defects was observed in all pre-heating conditions. Al and V segregation at microtwins was observed in the 100°C sample, reporting for the first time "selective" and mutually exclusive Al- and V-rich regions forming in adjacent twins. V segregation at dislocations was observed in the 570°C and 770°C samples, consistent with the higher preheating temperatures. High O contents were measured in all samples but with apparent opposing effects. At 100°C and 570°C was estimated to be below the critical threshold for O embrittlement and locally aids in maintaining a strength high by solid solution strengthening, whereas at 770°C it was above the threshold, therefore failing in a brittle fashion. Based on these observations, the initial increase in ductility from 100°C to 570°C is attributed to a reduction in microtwins and the dislocation networks acting as "soft barriers" for slip within a coarser microstructure; the latter also aids in maintaining a high strength. The lack of ductility at 770°C was attributed to local solute redistribution causing dislocation pinning and an increase of O content in this sample. Understanding of the microstructure evolution with increasing substrate temperature allows further

optimisation of LPBF produced Ti-6Al-4V, which will reduce the duration of post-processing and improving the mechanical properties, making it more attractive to industry.

## 1. Introduction

Laser Powder Bed Fusion (LPBF) is an additive manufacturing process where a high-intensity laser melts and fuses selected regions of powders deposited in cross-sectional layers. The near net-shape production of components minimises the need for specialised tooling and allows the manufacture of increasingly complex designs, better tailored to the requirements of specific applications. These characteristics are very attractive for manufacturing high-performance alloys in the aerospace industry. Titanium alloys, particularly Ti-6Al-4V, are used widely in the aerospace industry due to their high specific strength and hot corrosion resistance [1]. However, titanium alloys are expensive and time-consuming to produce using conventional cast and wrought methods [2]. LPBF is a viable alternative that allows the production of near-net shape bespoke components, reducing the cost and timeliness of substantial machining. However, several challenges have prevented this technology from reaching optimal commercial implementation. For instance, Ti-6Al-4V produced by LPBF reportedly showed reduced ductility and fatigue resistance compared with its counterpart produced by conventional methods [3]. This is due to the large temperature gradients and fast solidification rates which generates high residual stresses [4] and, more notably, the formation of highly textured, metastable martensitic structures [5].

Common strategies to improve the mechanical properties of LPBF Ti-6Al-4V relies on post-production heat treatments designed to decompose the martensitic structure [5]. For instance, Vilaro et al. [6] studied the microstructure produced by quenching from the  $\beta$  phase field and subsequent heat treatments at, above, and below the  $\beta$  transformation temperature (transus). The highest ductility values, but below conventional processing, were obtained when tempering close to the martensite start temperature ( $M_s$ ) and the resulting microstructure was a mixture of  $\alpha' + \beta + \alpha$  with lamellar morphologies. Other authors have found analogous microstructures and mechanical properties using similar heat treatments [7–9]. In addition, the use of multiple lasers in LPBF produced similar microstructures and mechanical properties [10]. Additional processes to reduce the residual stresses in LPBF produced materials include methods such as electropolishing [11] and hot isostatic pressing (HIP), which can also be used to reduce residual porosity [12]. These processes typically occur after an initial heat treatment [13].

In recent work, a heated base-plate was used during LPBF production of Ti64 to reduce residual stresses and decompose the martensitic structure [14]. Ali et al found an increase in ductility with increasing temperature between 100-570 °C, then a subsequent decrease up to 770 °C [14]. The present work employs advanced characterisation techniques, including SEM, TEM and APT, to correlate the changes in microstructures with elevated substrate temperature and loss in mechanical properties. It is found that complex phase transition sequences and solute redistribution behaviour control the final microstructure, and these are not comparable to standard LPBF techniques. Based on these observations, the mechanisms controlling the strength and ductility at different substrate temperatures are elucidated.

## 2. Experimental Methods

Gas-atomised powder of nominal chemical composition Ti-6Al-4V was provided by TLS Technik Spezialpulver and sieved to 15-45  $\mu\text{m}$  in diameter. The powders were used to manufacture 6 blocks, 30 x 30 x 10 mm in size, through LPBF on a pre-heated substrate at 100, 370, 470, 570, 670 and 770 °C. This was completed using a Renishaw SLM125 system with a modified pre-heating platform. The build was completed using the default Renishaw SLM parameters: laser focus offset 0, hatch spacing 0.08 mm, contour spacing 0.2, layer thickness 50  $\mu\text{m}$ , scanning strategy 90° alternative. The laser power and exposure time was varied between 120-200 W and 60-180  $\mu\text{s}$  respectively. Further details of production, residual stress measurements and porosity measurements have been

published as part of a previous manuscript [14].

## 2.1 X-ray diffraction (XRD)

X-ray diffraction (XRD) was carried out on the 100, 570 and 770 °C blocks to identify the bulk phases present using a Bruker D2 Phase diffractometer with Cu-K $\alpha$  (1.54184 Å) radiation. XRD was performed on the cross-section at the height of 4.5 mm of each selected Ti-6Al-4V block. These cross-sections were ground (600, 1200, 2000, 4000 grit) to ensure a flat surface. Scans covered  $2\theta$  angles from 25° to 100° with a tube voltage of 30 kV, current of 10 mA, a scanning step size of 0.035° and a dwell time of 0.8 s. Data was then processed using CrystalDiffract software and by comparing peak positions with data acquired from the Inorganic Chemistry Structure Database (ICSD). In case of peak overlaps, the deconvolution of peaks was performed by fitting Gaussian functions with the peak analyser tool in Origin 2019b with the background corrected and asymmetric least squares smoothing. The centre of each measured peak was compared and matched with the reflexion list of the theoretical pattern for each phase, generated using commercial crystallographic analysis software CrystalDiffract, and the dominant phase within each overlapping peak was determined with the relative intensity of the fitted peaks.

## 2.2 Metallographic preparation and imaging

Samples were sectioned for metallographic examination using a diamond saw, then hot-mounted in conductive bakelite (with carbon filler), polished initially with SiC grinding paper, then with 3 and 1  $\mu\text{m}$  diamond paste and finally 0.04  $\mu\text{m}$  colloidal silica to obtain a smooth surface finish. Scanning Electron Microscopy (SEM) was performed on sections of the samples using a Zeiss GeminiSEM 300 microscope. A working distance of 8.5 mm was used, operating at a beam current of 3 nA and a voltage of 5 kV. A combination of secondary and backscattered electron imaging was used, in order to fully exploit the surface sensitivity and Z-contrast. Fracture surfaces were also observed (without mounting and polishing) using the same SEM parameters, except increasing the working distance to 20-25 mm for an improved depth of field. Electron backscatter diffraction (EBSD) measurements were performed with a Bruker eFlash<sub>HD</sub> EBSD camera inside a FEI Quanta 650 scanning electron microscopy (SEM) using a beam acceleration voltage of 20 kV and a probe current of ~10 nA. Each sample was analysed with an EBSP resolution of 320x240 pixels, samples at 570 and 770 °C were analysed with a step size of 40 nm and an EBSD camera exposure of 25 ms while the sample at 100 °C was captured with a step size of 200 nm and an EBSD camera exposure of 70 ms.

## 2.3 Transmission electron microscopy (TEM)

Transmission electron microscopy (TEM) was performed on 3 mm disc samples, which were cut using a diamond saw, then electropolished using a Struers Tenupol with a solution of 15% (by volume) perchloric acid in methanol, cooled with LN<sub>2</sub>. Each specimen was examined using a Technai Osiris microscope with a Bruker Energy Dispersive X-ray detector (EDX). Diffraction patterns were obtained, however, very often the particles present in the microstructure were too small to use the smallest selected area aperture. Convergent beam diffraction had to be performed using the smallest spot sizes, which, when converged, allowed diffraction patterns to be taken from microstructural features smaller than ~40 nm. From the micrographs acquired, particle size distributions were determined through manual measurements. Data is presented as means and standard deviations. The matrix compositions of each specimen were measured by TEM-EDX, and any values presented here were obtained by taking the mean value over at least 10 measurements. Semi-quantitative data was obtained from EDX maps using the Cliff-Lorimer method.

## 2.4 Atom probe tomography (APT)

Atom probe tomography (APT) was performed on the samples using a LEAP 5000 XS in laser-pulsing mode. Specimens were prepared by in-situ lift out using a FEI Helios NanoLAB 600i dual-beam SEM-FIB, equipped with an Omniprobe micromanipulator. The Ga beam was used to prepare cantilevers, which were then welded onto the micromanipulator using Ga-beam deposited Pt, extracted and mounted onto Cameca Silicon flat-top coupons. Specimens were then sharpened using the Ga-beam until they were below 100 nm in diameter, then cleaned using 5 kV Gallium, to remove the region minimise the ion beam damage. Analysis conditions were varied based on the specimen's profile within a selected range: temperatures between 40–60 K, Laser energy in the range of 10–30 pJ, and a pulse frequency between 100 and 200 kHz. Reconstructions were performed using the Cameca Integrated Visualisation and Analysis Software IVAS 3.8.4 software.

## 2.5 Tensile testing

Finally, tensile tests were performed at room temperature using an Instron quasi-static servo-hydraulic mechanical tester at a constant strain rate of  $10^{-4} \text{ s}^{-1}$ , measured by means of an extensometer. The 3 repeat tests were performed for each condition. Details of the mechanical tests can be found in previously published work [14].

## 2.6 Pore characterisation

Fractography was performed on the samples after mechanical testing to assess porosity levels, determine fracture initiation points and observe the relative microstructures of the fracture surfaces. **Figure 1** shows secondary electron micrographs which were used to determine the porosity levels in the samples produced by LPBF with substrate temperature of 100, 570 and 770 °C respectively.

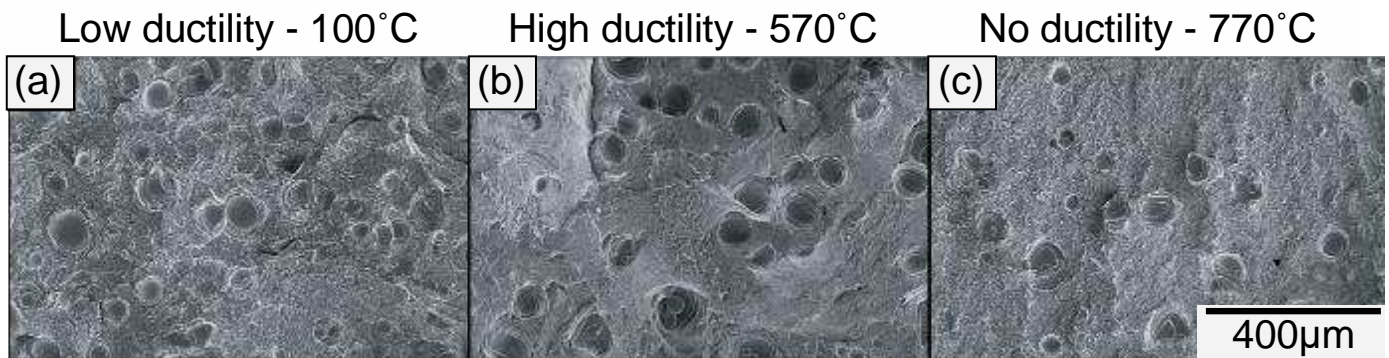


**Figure 1:** Secondary electron micrographs obtained of the fracture surfaces of each tensile tested sample, showing pore size and fraction. (a) 100 °C , (b) 570 °C and (c) 770 °C.

To verify that porosity was not a factor affecting the mechanical behaviour of the samples at these temperatures, the pore sizes were estimated with ImageJ. A total of at least 60 pores per sample were measured. Following the method outlined by Ashby [15], stereology structure factors were calculated by assuming that all the pores were spherical and that the measurements were obtained from planar surfaces. The pores can be assumed to be spherical, as spherical porosity is characteristic of over melting due to excess heat input and potential initiation of key-hole type melting [], as seen by the spherical type nature of the pores in **Figure 1**. The pore sizes were calculated by using the following geometric formula:

$$r_v = \sqrt{\frac{3}{2}} r_s$$

### Equation 1

Where  $r_s$  is the mean radius of intersection with a 2D planar surface, and  $r_v$  is the mean 3D pore radius.

The number of particles intersecting a unit area  $N_s$  was then measured and used to calculate the volume fraction,  $f$ , using:

$$f = N_s \frac{2}{3} \pi r_v^2$$

### Equation 2

$N_s$  was calculated by taking a SEM fractography micrograph with a low magnification and counting the number of pores in the micrograph. The number of pores was then divided by the area of the micrograph to obtain  $N_s$ .

## 3. Results

### 3.1 Mechanical data and fractography

Mechanical test results were published as part of a previous study [14] discussing the methods for alleviating internal stresses caused by additive layer manufacturing through heat treatments. **Figure 2 (a)** summarises the values of ductility and how they are influenced by the substrate temperature. When the substrate is heated to 100°C, the baseline elongation is ~6%, which increases and peaks at ~10% at 570°C, then sharply decreases to 0% (brittle failure, no ductility) at 770°C. **Figure 2 (b)** shows the change in ultimate tensile stress (UTS) with respect to substrate temperature. It can be seen that above 670°C there is a sharp decrease in the UTS of the material, which can be related to the similar loss in ductility, due to brittle failure.

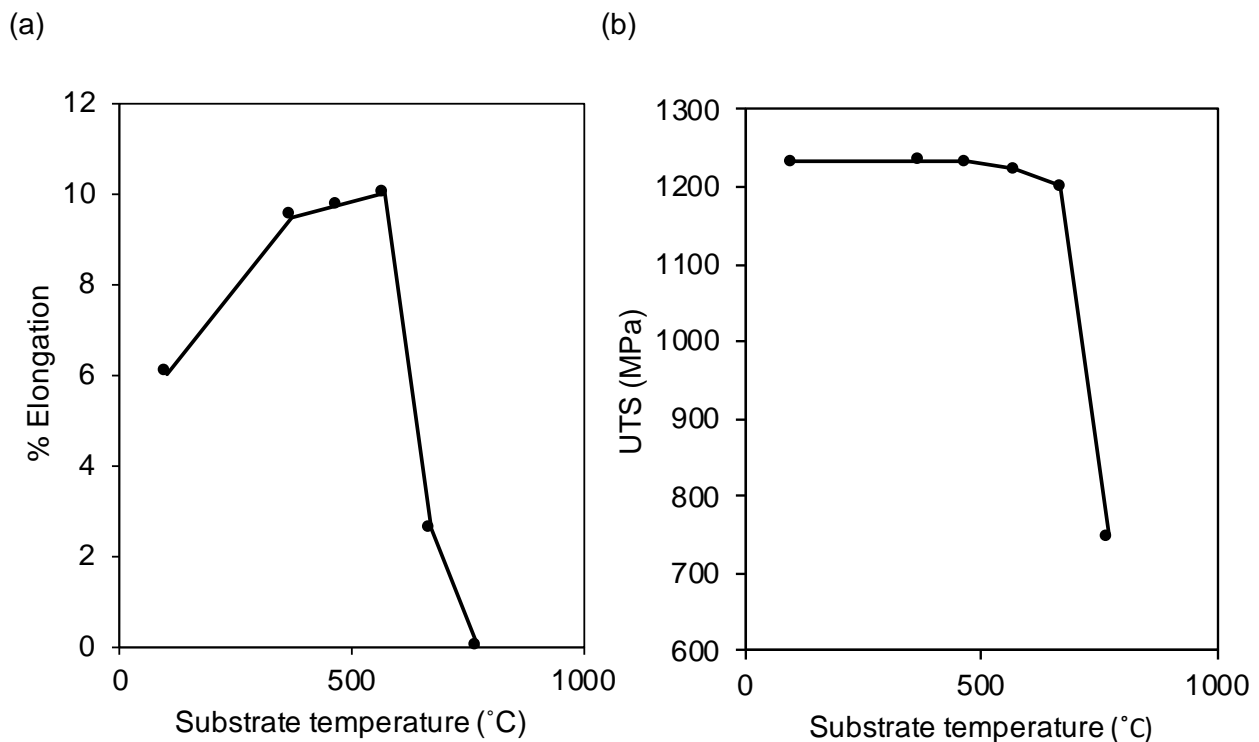


**Figure 2:** (a) % elongation vs substrate temperature during LPBF processing, measured during room temperature tensile tests, performed at  $10^{-4}$  s $^{-1}$  strain rate. The sample made by pre-heating the powder bed at 770 °C was brittle. (b) ultimate tensile strength (UTS) vs substrate temperature.

The distribution of the 3D pore radius is plotted in a histogram, as shown in **Figure 3**. It was found that the largest pores (>100  $\mu\text{m}$ ) were present in the 570  $^{\circ}\text{C}$  sample. The 770  $^{\circ}\text{C}$  sample shows a more conservative distribution, with frequencies of pore sizes tending to be smaller. At 100  $^{\circ}\text{C}$  the pore radius is most frequent from 0.04-0.07 mm.

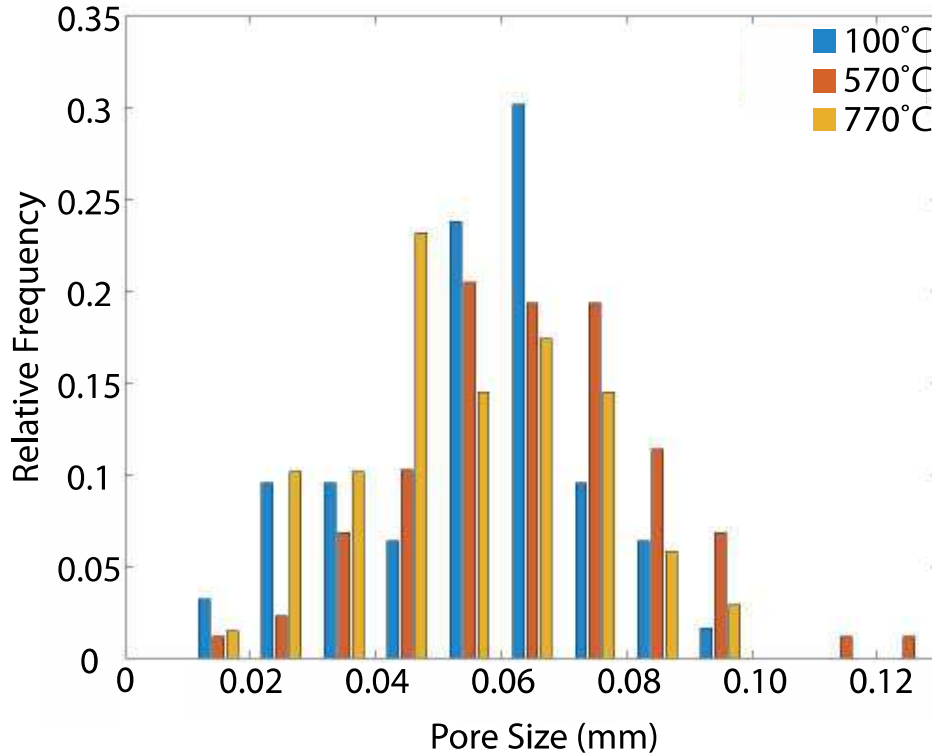


**Figure 3:** Distribution of pore radii.

The mean pore radius  $r_v$ , number of pores per unit area  $N_s$ , and volume fraction are tabulated in **Table 1**. The largest average pore radius is found in the 570  $^{\circ}\text{C}$  sample, with the 100  $^{\circ}\text{C}$  and 770  $^{\circ}\text{C}$  measuring a similar pore radius. However, the 100  $^{\circ}\text{C}$  has significantly more pores per unit area than the other two temperatures. The volume fraction of the pores decreases with increasing temperature. Both the alterations in pore parameters and drastic change in tensile properties must be explained through thorough characterisation of the sample microstructures.

**Table 1:** Pore parameters and volume fraction for the 100  $^{\circ}\text{C}$ , 570  $^{\circ}\text{C}$ , and 770  $^{\circ}\text{C}$  samples

	100 $^{\circ}\text{C}$	570 $^{\circ}\text{C}$	770 $^{\circ}\text{C}$
$r_v / \mu\text{m}$	55.9	64.1	54.7
$N_s / \text{mm}^{-2}$	64.1	39.7	39.1
Volume fraction, $f$	0.419	0.342	0.245

### 3.2 Microstructural characterisation of the undeformed samples

In order to identify the primary deformation and failure mechanisms, microstructural characterisation was performed. Initially, bulk phases were identified by XRD, as shown in **Figure 4**. XRD was able to identify the following phases at each temperature:  $\alpha$ -Ti,  $\beta$ -Ti and  $\alpha'$ -Ti.  $\beta$ -Ti was only identifiable

by XRD in the 570°C and 770°C sample, with more peaks corresponding to  $\alpha$ -Ti with increasing temperature.

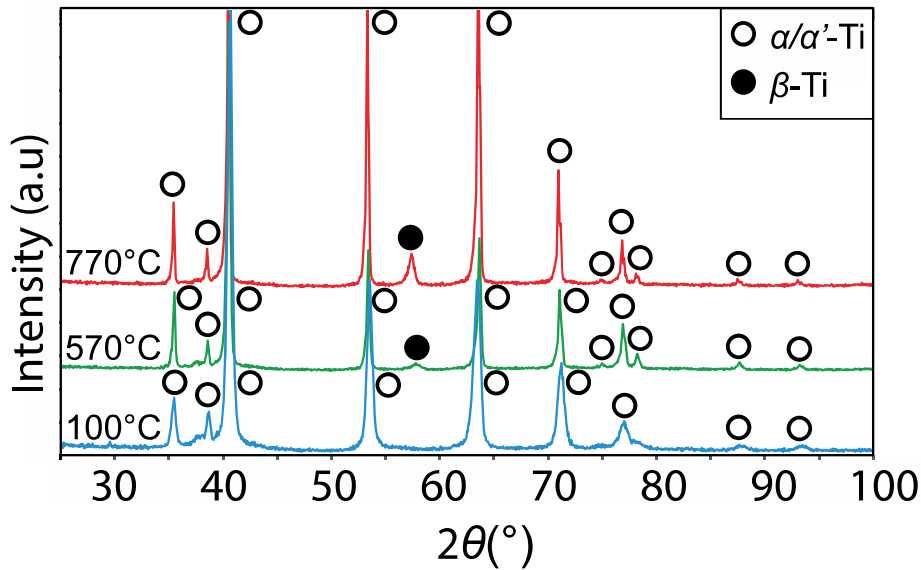


**Figure 4:** X-ray diffractograms performed to obtain the phase composition at room temperature of Ti6Al4V samples which were 3D printed on a pre-heated powder bed. The peaks are annotated with the corresponding dominant phase based on the fitted Gaussian function peak position.

The typical microstructural features observed at the  $\mu\text{m}$  length scale- are shown in **Figure 5** with backscattered electron micrographs of the microstructures produced through printing at 100, 570 and 770°C (as-built, non-tensile tested). When samples are built on a heated substrate at 100°C, only  $\alpha$  and  $\alpha'$  phases are visible, in the form of columnar grains [16], with small flecks of retained  $\beta$  phase. There is less martensitic  $\alpha'$  in the sample produced at 570°C but it appears there is slightly more retained  $\beta$  within this microstructure. At 770°C, there is significantly less martensitic  $\alpha'$ , with larger lamellar  $\alpha$  grains, with significantly more retained  $\beta$  within the matrix.

EBSD was performed on the samples to better identify the phases observed by SEM in **Figure 5**. When building a sample on a heated substrate at 100°C, the microstructure consisted primarily of  $\alpha$  and  $\alpha'$  phases (as  $\alpha$  and  $\alpha'$  have too similar a lattice parameter and crystal structure, regular EBSD could not be used to differentiate between them). Small pockets of  $\beta$  phase could be identified, though the low volume fraction explains its absence from the X-ray diffractograms in **Figure 4**. EBSD also showed extensive presence of microtwins in the 100°C sample. In comparison, the sample produced on a heated substrate at 570°C showed no alterations in grain size  $\beta$  phase fraction, though this time a complete absence of microtwins was recorded. At 770°C no twins were visible and the  $\alpha$  grain size increased.

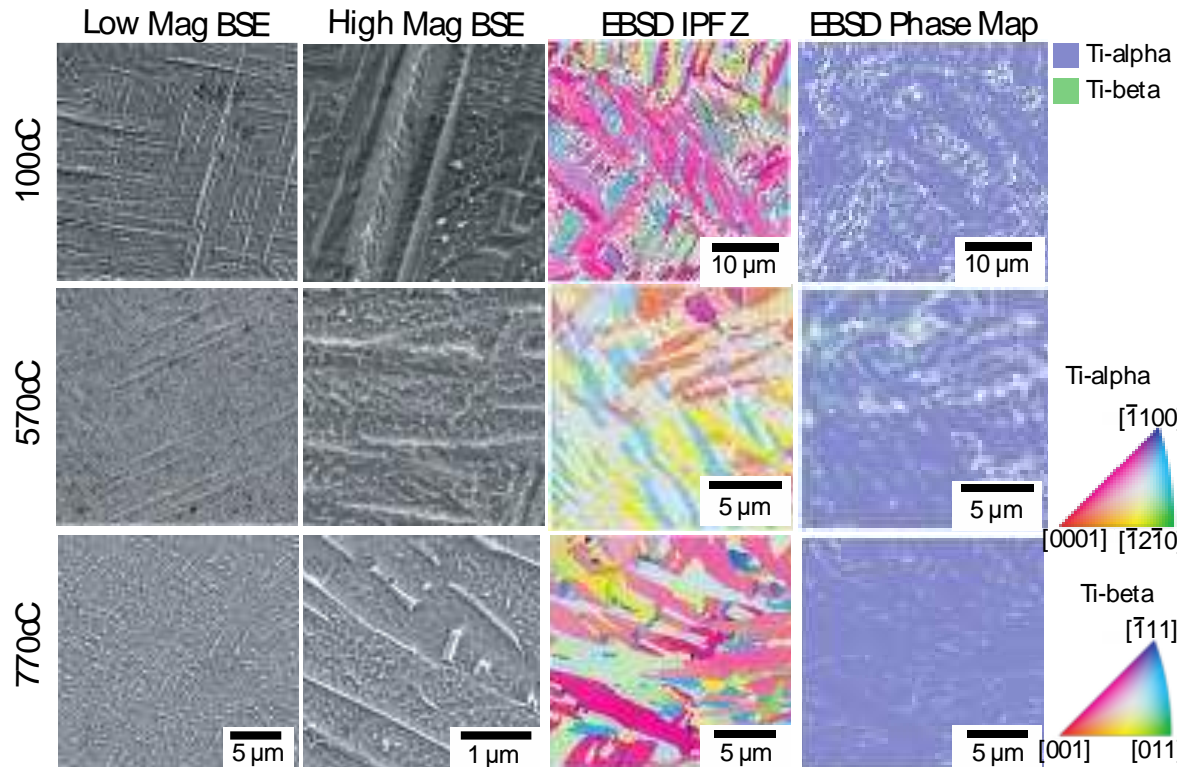


**Figure 5.** Backscattered electron micrographs showing the overall microstructure of the 3D printed samples and details of the phases present at higher magnification. Micrographs were taken from a central region of the x-z axis (vertical sections). EBSD inverse pole figure (IPF) maps along the x-axis and a phase fraction map for each sample.

### 3.3 Compositional analysis and fine scale microstructure

Bright field TEM and EDX was performed on the samples and the results are shown in **Figures 6 to 8**. **Figure 6** are micrographs and EDX maps of the sample produced at 100°C. Microtwins are visible, which is consistent with the results shown in **Figure 5**. EDX maps could not resolve a possible segregation of solutes at the microtwin boundaries.

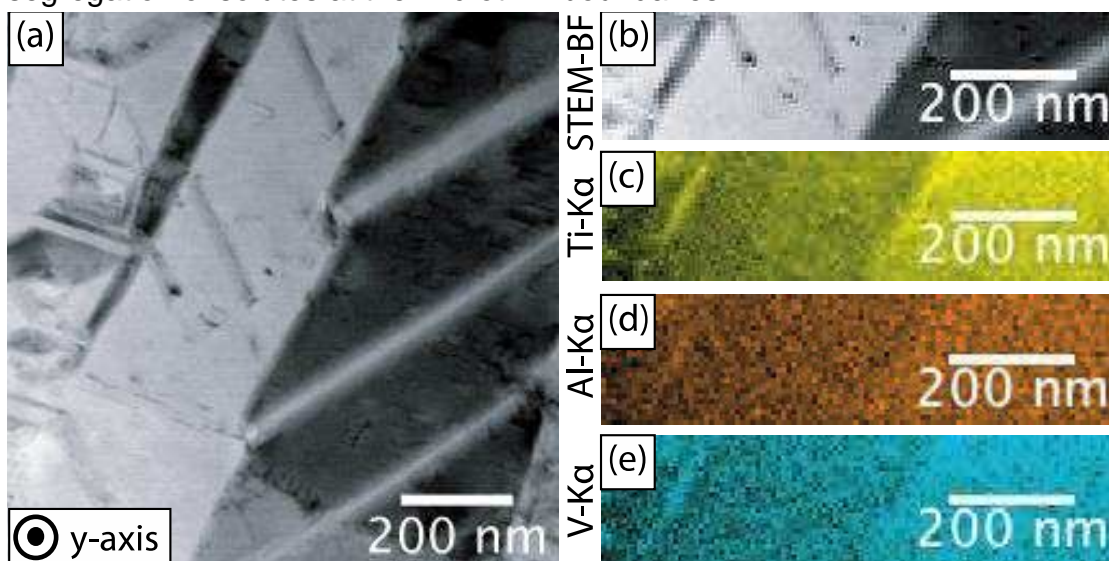


**Figure 6:** TEM/EDX results of the sample produced at 100°C. (a) STEM –BF of 100°C sample; (b) Magnified STEM-BF; (c) Ti-K $\alpha$ ; (d) Al-K $\alpha$ ; (e) V-K $\alpha$

The sample produced at 570°C showed no microtwin boundaries (**Figure 7**) but EDX maps showed small quantities of nano-scale  $\beta$  particles (shown by the rejection of V from the  $\alpha$  phase in the EDX) which were too small to be identified by EBSD in **Figure 5**, though there is a presence of dislocations which is not seen in the 100 °C specimen. The dislocations are more substantial within the  $\alpha$  lamellae.

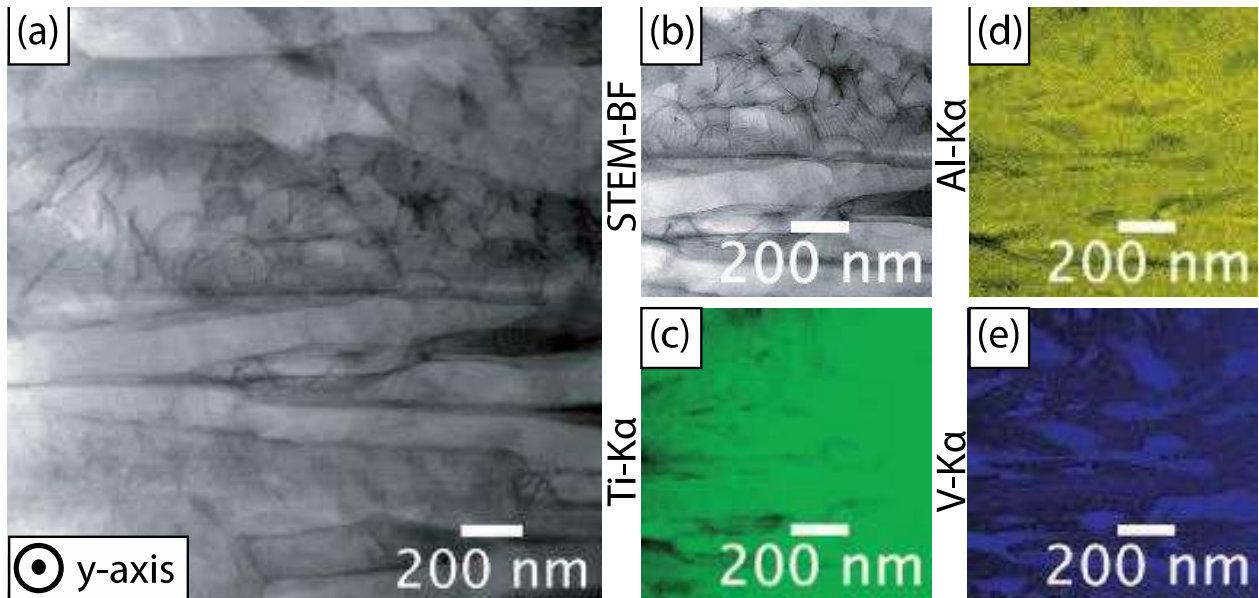


**Figure 7:** TEM/EDX results of the sample produced at 570°C. (a) STEM –BF of 570°C sample; (b) Magnified STEM-BF; (c) Ti-K $\alpha$ ; (d) Al-K $\alpha$ ; (e) V-K $\alpha$

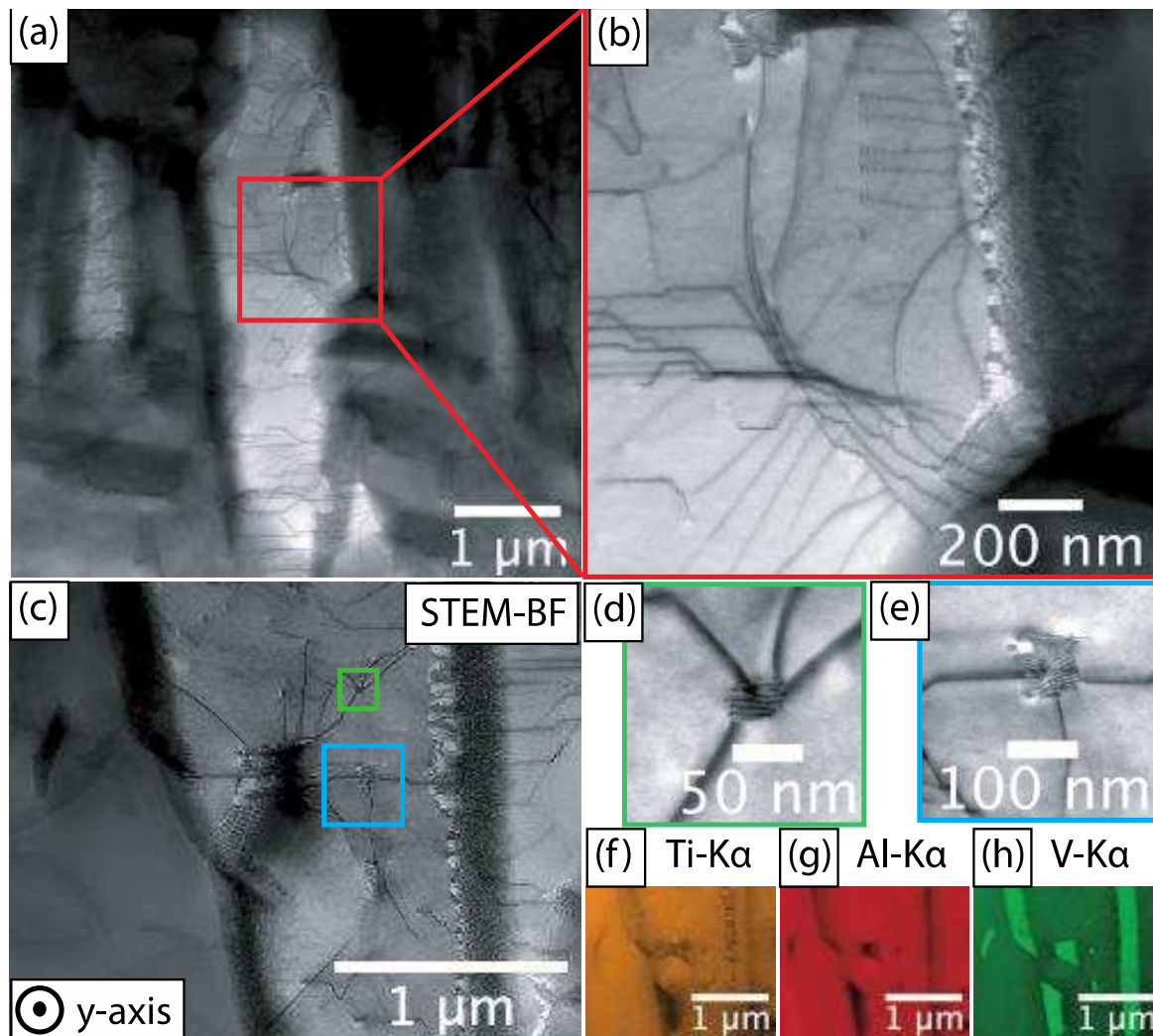


**Figure 8:** TEM/EDX results of the sample produced at 770°C. (a) STEM –BF of 770°C sample at low magnification to show  $\beta$  grain; (b) Magnified STEM-BF to show dislocation along preferential planes; (c) STEM –BF with (d-e) magnified view of two  $\beta$ -Ti precipitates; (f) Ti-K $\alpha$ ; (g) Al-K $\alpha$ ; (h) V-K $\alpha$

The sample produced at 770°C also had nano-scale faceted  $\beta$  precipitates (**Figure 8**). **Figure 8(a) and (b)** also showed networks of dislocations, tangled and evidently cross-slipped along specific crystal orientations, which is visible from the 60° angles between them (in this observed axis). **Figures 8 (c) to (h)** show the nano-scale  $\beta$  precipitates, which do not appear to be retained  $\beta$  from an  $\alpha$  to  $\beta$  phase transformation. **Figures 8 (f) to (h)** also shows that the dislocations have segregation of V and that V-rich precipitates, such as nano- $\beta$  phases could be either pinning dislocations or forming at the intersection between them.

### 3.4 Fine scale phase segregation

In order to investigate the fine scale compositional variations, atom probe tomography was used. **Figure 9** shows an atom probe reconstruction from each sample. The local concentration of V and Al is shown as the iso-concentration surfaces of 4 at% and 12 at% respectively, to allow a distinction between the  $\alpha'$ -Ti and  $\alpha$ -Ti phases, which have the same crystal structure but differ in chemical composition and lattice parameter [17]. The change in the relative amounts of  $\alpha'$ -Ti and  $\alpha$ -Ti across the three samples, especially between **Figure 9 (a) and (c)**, substantiates the XRD results showing that the amount of  $\alpha'$ -Ti decreases with temperature, despite the reduced sampling volume available in APT studies.

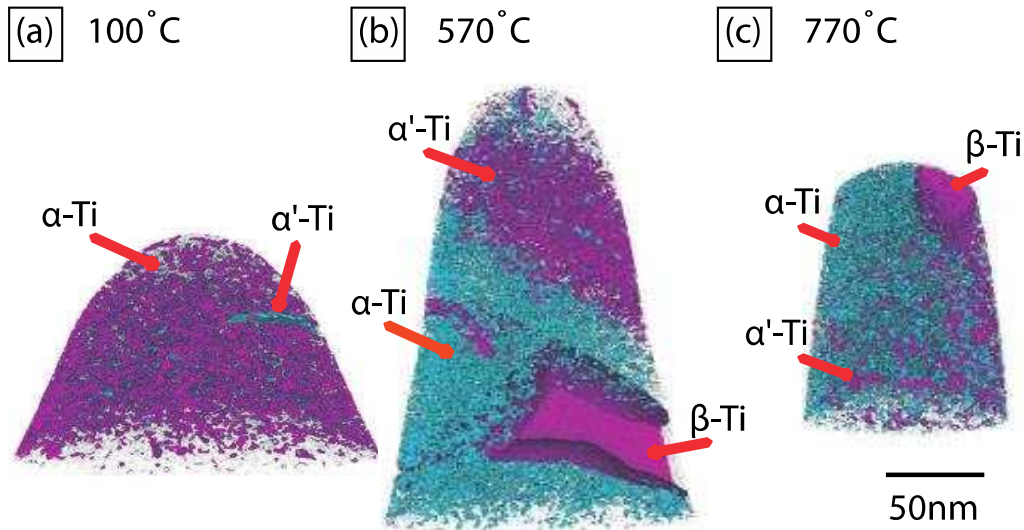


**Figure 9:** APT reconstruction of the three samples. Isosurfaces of 4 at.% V and 12 at.% Al were applied. The 570°C sample (b) shows the clearest segregation of phases, while the 100°C sample (a) and 770°C sample (c) shows a majority of  $\alpha'$ -Ti and  $\alpha$ -Ti microstructure, respectively.

In order to obtain a reliable breakdown of the elemental composition of each phase, a peak decomposition algorithm was used. This separates the contribution of each constituting element when two peaks overlap by using the natural abundances of isotopes of each element respectively. The composition values obtained for  $\alpha$ ,  $\beta$  and  $\alpha'$  measured on the sample produced by substrate at 570°C, were compared to the literature for similar samples, albeit produced without the heated substrate. Furthermore, the other vanadium and aluminium-rich regions labelled in **Figure 9(b)** as  $\alpha$  and  $\alpha'$ , matched the composition of  $\alpha$ -Ti and  $\alpha'$ -Ti found by Tan et al. [5] from observation of the 1D concentration profile. The composition of the three phases is tabulated in **Table 2**, while the individual locations of phases are labelled in **Figure 9(b)**. **Table 2** also confirms the absence of  $\beta$ -Ti in the 100°C sample as the composition of vanadium ( $\beta$  stabilising element) does not exceed 5 at.%. The XRD analysis indicates a shift of the  $\beta$ -(002) reflection towards higher  $2\theta$  (**Figure 4**) which would result from a reduction of the  $\beta$ -lattice parameter. This reduction can be associated with an increase of the V-concentration in the  $\beta$ -phase as shown in **Table 2** [18].

**Table 2.** Compositions (in at.%) of  $\alpha'$ -Ti,  $\alpha$ -Ti and  $\beta$ -Ti phases obtained from APT data. \* denotes the use of a 1D concentration profile instead of decomposition of peaks, while ^ denotes the use of decomposition of peaks but with interfaces created by iso-concentration surfaces.

Element	Alpha			Alpha Prime			Beta	
	100°C*	570°C	770°C^	100°C*	570°C	770°C^	570°C	770°C
Ti	bal.	bal.	bal.	bal.	bal.	bal.	bal.	bal.
Al	11.19	10.46	14.79	6.92	9.59	10.94	2.79	1.72
V	3.21	2.37	2.30	3.85	3.69	5.13	22.69	23.79
Cr	0.13	0.28	0.20	0.14	0.77	0.91	0.72	0.16
O	0.69	0.76	0.90	0.67	0.74	1.26	0.06	0.07
Fe	0.49	0.00	0.07	0.40	0.02	0.04	4.54	3.03

### 3.5 $\beta$ phase partitioning at 570°C

A proximity histogram, in **Figure 10(b)**, applied across the  $\beta$ -Ti phase reveals solute partitioning with Ti, Al, and O preferentially partitioning to the  $\alpha$ -Ti phase while V is a  $\beta$ -Ti phase stabiliser. This matches Conrad's [19] findings that oxygen and nitrogen are  $\alpha$ -Ti stabilisers and preferentially partition to the  $\alpha$ -phase. A cylinder ROI was applied along a region of high vanadium concentration just next to the large  $\beta$ -Ti grain as indicated with an arrow to illustrate the solute segregation at an interface. This region of high concentration is parallel to the grain boundary of the large  $\beta$ -Ti grain and could be part of a smaller  $\beta$ -Ti grain that is located beyond the sample lifted out. 0.1 at% V and trace (<0.01 at%) concentrations of Fe were detected along linear features assumed to be dislocations in the data set shown in **Figure 10** [20,21]. At the assumed dislocation, the measured ionic composition of  $O_+$  is estimated as  $0.016 < 0.020 < 0.024$  ionic% (95% confidence interval). There is, however, a known peak overlap of  $TiO_+$  and  $O_+$  which could allow the underestimate of oxygen content. The peak overlap was analysed further using a custom Matlab program to enable localised (3D) isotopic deconvolution to improve accuracy of atom probe data measurements despite a known local overlap. This analysis showed that there is ~80 times more O from  $TiO_+$  than  $O_+$  and in this case the error can be ignored.

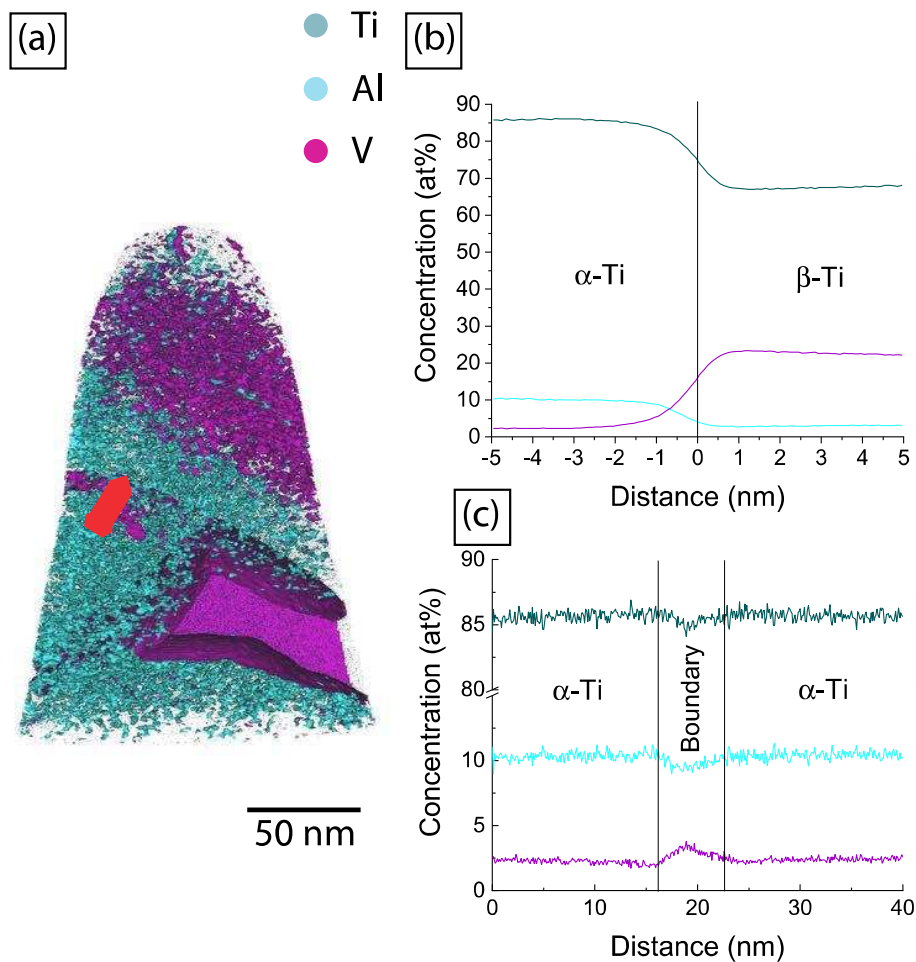


**Figure 10:** APT reconstruction of the 570°C sample (a) with iso-concentration surfaces of 4at% V and 12at% Al applied, and the location of the cylinder region of interest (ROI) demarcated with an arrow. (b) shows the proximity histogram about the large  $\beta$ -Ti grain on the bottom right of the sample, while (c) is a 1D concentration profile of the cylinder ROI indicated in (a).

### 3.6 Segregation of microtwins at 100°C

Iso-density surfaces were applied to the reconstructions of the samples produced at 100°C and 770°C, to explore other microstructural features which would not be evident in atom probe reconstructions in the absence of solute segregation, such as dislocations, grain boundaries, twin boundaries, etc which the TEM micrographs suggested were segregated with Ti and V, as shown in **Figure 6(a)** and **(g)**. The density iso-surfaces of aluminium and vanadium in **Figure 11(a)** reveal planar surfaces that appear to only be in specific directions, at ~60° angles from each other, as would be expected of twin boundaries. This suggests that the planes follow specific crystallographic planes and together with the micrographs in **Figure 7(a)**, it suggests that these are boundaries of twins. The 1D concentration profiles in **Figure 11(b)** and **(c)** reveal that there is both vanadium and aluminium segregation at each twin boundary.

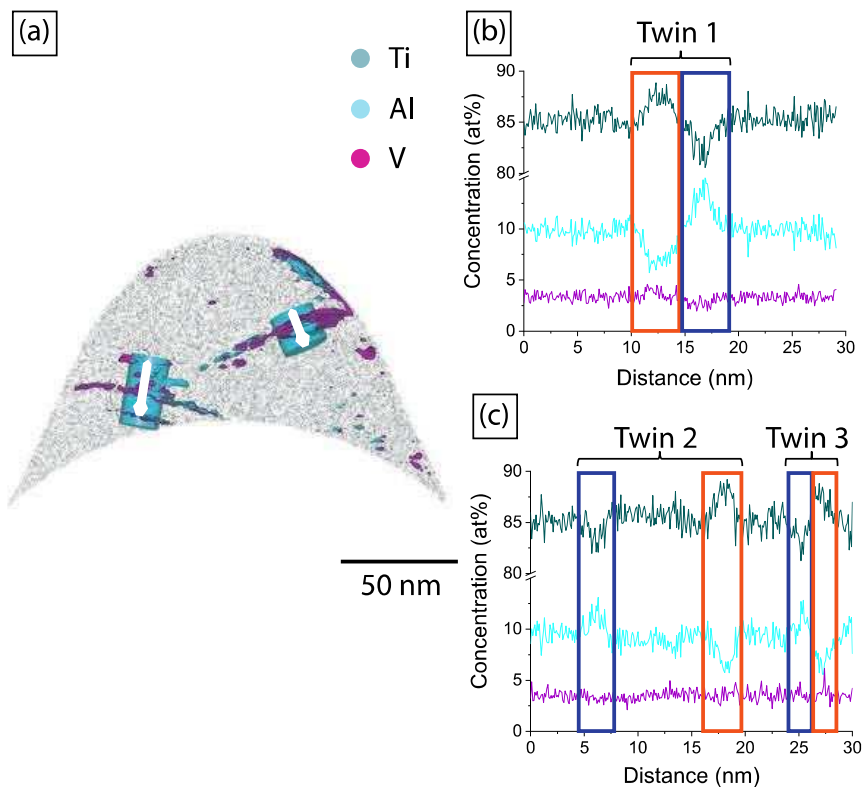


**Figure 11:** (a) Density iso-surfaces of vanadium 2.65/nm<sup>3</sup> (magenta) and aluminium 6.90/nm<sup>3</sup> (turquoise) were applied to the 100°C sample. Two cylindrical ROIs were added to investigate the planar surfaces. (b) and (c) show the 1D concentration profile of the two ROIs with their corresponding variation in elemental composition.

### 3.7 Segregation to dislocations at 770°C

In the reconstruction of the sample produced at 770°C, titanium and vanadium isosurfaces delineating regions of high point density were added to reveal the segregation to linear features, which are assumed to be dislocations [20,21], which could be contributing to pinning and therefore lack of mobility, as observed in the TEM in **Figure 8(c)** to **(f)**. A  $\beta$ -Ti particle can be observed at the top right of the sample, with high-density columnar titanium regions oriented along the z-axis of the sample. The rod-like shape, coupled with the segregation matching the observations performed by TEM, suggests that these are dislocations, while the large quantity of high-density titanium region suggests a significant increase in dislocation density at 770°C. The 1D composition profile in **Figure 12(c)** helps to quantify the changes in composition detected by the TEM-EDS. It is noted that a similar feature to that of the vanadium rich grain boundary like planar feature is also found next to

the  $\beta$ -Ti grain as per the 570°C sample. It is noted that the amount of oxygen in the reconstructions has increased with printing powder bed temperature and could play a role in affecting the mechanical behaviour of the samples.

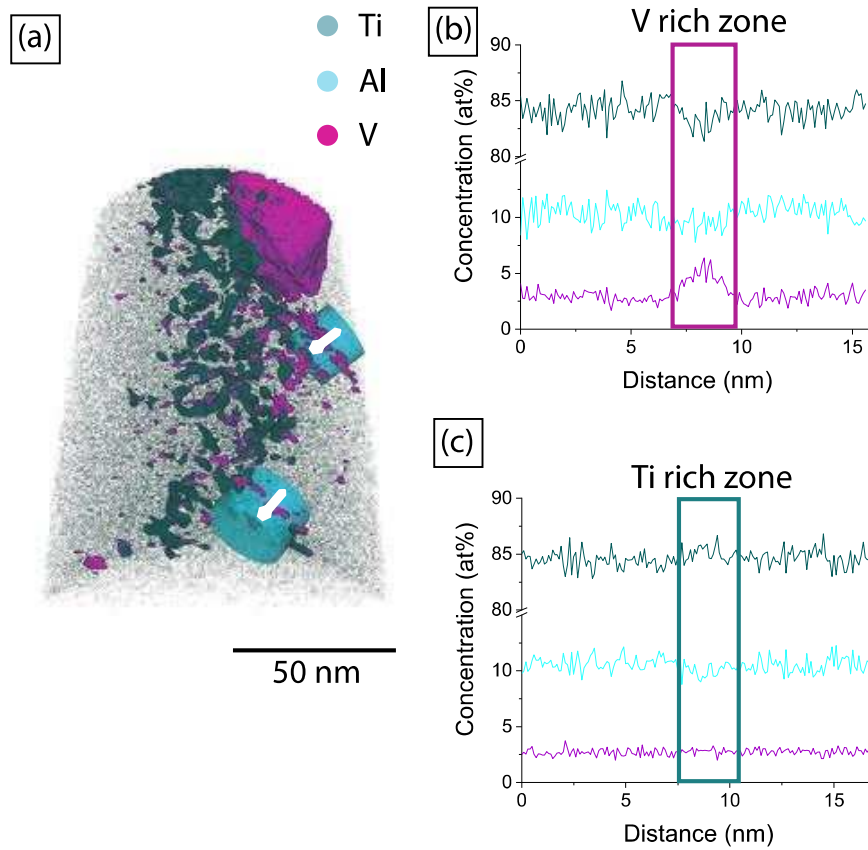


**Figure 12:** (a) Density isosurfaces of vanadium  $2.00/\text{nm}^3$  (magenta) and titanium  $51.50/\text{nm}^3$  were applied to the  $770^\circ\text{C}$  sample. Two cylindrical ROIs were added to investigate a high-density vanadium region next to the  $\beta$ -Ti grain on the top right and the high-density titanium region, with their 1D concentration profiles plotted in (b) and (c) respectively.

## 4. Discussion

### 4.1 Porosity and relation with mechanical properties

**Table 1** shows that the volume fraction of pores decreases with temperature and therefore a reduction in ductility cannot be explained by the change in porosity. The corresponding difference in UTS, as well as the change in ductility is therefore a result of microstructural differences. It can be presumed that the sample preferentially fractured at pores, giving a 'non-random' crack path and introducing error into the measurement of porosity. However, this is assumed to be negligible. It is also noted that the SEM image used to calculate the number of pores in a unit area for the  $570^\circ\text{C}$  had a significant region where porosity was absent. Thus, the recorded porosity for  $570^\circ\text{C}$  obtained might be lower than present in the sample due to this sampling bias. As a point of comparison, Leuders et al. [11] detected a porosity of 0.23 in LPBF specimens using X-ray tomography, and pore sizes were reported to range from  $50\ \mu\text{m}$  to  $300\ \mu\text{m}$  [22]. In the present work, the experimental volume fraction of porosity is higher than that measured by Liu and Shin. This may be due to the measurements being performed on tensile specimens as the pores might have coalesced during the fracture process. However this may be negligible as there is not significant elongation to failure, and therefore pore growth would not be substantial.

## 4.2 Effect of substrate temperature in microstructure evolution

One of the most interesting results from this work is the significant and somewhat surprising differences in the microstructure when varying the substrate temperatures. Table 3 summarises such changes. At 100°C, very little  $\beta$  forms and there is a large phase fraction of  $\alpha'$ . Additionally, there are significantly more pores per unit area, with the highest volume fraction of pores of all the tested samples. The microstructure contains both  $\alpha$  and  $\alpha'$ , and has a lower dislocation density than the other two conditions. The rapid cooling rate upon solidification provides necessary driving force for large scale  $\beta$  to  $\alpha'$  transformation [23,24] and shows a fast cooling microstructure with the presence of microtwins [25]. The very low fraction of  $\beta$  phase is likely due to rapid solidification and little diffusion at 100°C preventing its formation. In addition, there is a presence of microtwins with both Al and V rich regions, though there is not both Al and V rich regions together at the interface. This indicates that short range diffusion is occurring due to the formation of these microtwins within the alloy, which could be due to a partitioning effect towards forming  $\alpha$  and  $\beta$  in the Al- and V-rich regions; this mechanism has been seen experimentally in other alloy systems [26,27]. Microtwins are a result of the high lattice strains and low symmetry between the  $\alpha$  and  $\beta$  phases [28], therefore chemical segregation occurs.

**Table 4.** Predicted local Al, V and O concentrations at crystal defects and their influence on local variations in solid solution strengthening.

	100 °C	570 °C	770 °C
Primary phases	$\alpha'+\alpha$	$\alpha'+\alpha+(\text{nano})\beta$	$\alpha+\beta$
Porosity fraction (%)	highest	medium	lowest
Crystal defects	Twinning	Dislocation networks	Dislocation tangles
Solute behaviour	Al, V segregation at twins	V segregation at dislocations	V segregation at dislocations

Upon increasing the substrate temperature to 570°C, there is no longer evidence of microtwinning. Instead, nano-scale  $\beta$  are observed within  $\alpha'$  and  $\alpha$ . Though the largest pore radius is seen at this temperature, the ductility is the highest of all 3 samples discussed here. Dislocation networks were observed within the  $\alpha$  lamellae, which may be due to the absence of microtwinning and the presence of  $\beta$  at the  $\alpha$ -grain boundaries. Interfacial dislocations in Ti-6Al-4V may form at the (moving)  $\alpha'/\beta$  interface as  $\alpha'$  nucleates and grows during rapid solidification in the first build cycle, due to the high shear strain of the martensitic transformation and the high local lattice mismatch between  $\alpha'$ ,  $\alpha$  and  $\beta$  phases. The substrate temperature is high enough to promote dislocation recovery, however the remnant  $\beta$  at the grain-boundary should inhibit significant dislocation annihilation and local dislocation reconfiguration could take place instead. As for how the networks influence mechanical properties, they could act as “soft barriers” for slip [27]. Using the analogy of dislocation networks forming in single-crystal (SX) Ni-based superalloys, Rai et al. have observed that the formation of dislocation networks at the  $\gamma/\gamma'$  interfaces promotes strain localisation and material softening under low-cycle fatigue [29]; the deformation temperature was 850°C, which is sufficiently low to prevent directional coarsening and dislocation reconfiguration was primarily driven by the interfacial misfit and deformation within the matrix. This indicates that in the present case, the dislocation networks promote an increase in ductility by allowing more plasticity to take place locally within the  $\alpha$  lamellae, whereas the fine grain boundaries and nano- $\beta$  should compensate for the local softening and keep the macroscopic strength high. In addition, the micro texture of the alloy from the EBSD shown in **Figure 5** indicates that there may be  $\langle a \rangle$  type dislocations which could be transferred easily between  $\alpha$  lamellae, which may be further increasing the ductility of the material, however this is similar in all samples and is often found in similar titanium microstructures [30,31].

At 770°C, there is a significant change in mechanical properties and this is reflected also in the dislocation content and phase structure. A rapid drop in ductility is observed, despite the specimen

containing the smallest pores. There is substantially more  $\beta$  within this sample and very little  $\alpha'$  remains, however, this should not lead to such a large loss in ductility. Dislocation tangles are observed in **Figure 8**; these could be formed by a similar mechanism as the dislocation networks at 570°C but the higher build temperatures could promote extensive recovery and partial loss of the networks; the high density of dislocation networks observed in the vicinity of the  $\alpha/\beta$  interface in **Figure 8** supports this mechanisms, as grain-boundary  $\beta$  should limit the extent of dislocation recovery by maintaining the interfacial misfit. The lack of ductility in this sample indicates that the dislocation structures are no longer acting as soft barriers for dislocations and additional mechanisms are operating which could hinder slip. The fact that V-rich dislocations are observed (**Figure 12**) indicates that solute redistribution is playing an important role in controlling dislocation slip, however it could also be stated that O has a role to play in leading to such a brittle sample [32].

The presence of H and/or O due to process-related contamination could affect strongly the elongation at 770°C, as these elements are well known to promote substantial reductions in ductility in titanium alloys [33]. It is common for samples produced via SLM to contain increased oxygen content, particularly within the  $\alpha'$  phase [34]. For instance, Tan et al. [5] measured high H and O levels (between 0.1-1 at%) in Ti-6Al-4V produced by EPBF. Oxygen content was quantified through atom probe tomography (APT). APT was used to identify microstructural features according to their chemical composition and quantify the elemental segregation at interfaces and dislocations observed in the TEM in **Figure 6 to 8**. It has also been previously indicated that oxygen increases the critical stress for martensite formation, and increased oxygen content may suppress martensite formation. As increased substrate temperatures have less martensite, this could indicate that heating the substrate results in higher oxygen contents of the alloy [35]. The presence of any number of elements may aid the atomic shuffle required for the martensitic transformation, and therefore local composition is highly important.

#### **4.2.1. Comparing against microstructures obtained by other Additive Manufacturing methods**

To understand better how the preheating temperatures affect local changes in thermal history and microstructure, it is worth comparing the results from this work with results obtained by processing Ti-6Al-4V using other AM technologies. At 100 °C, the microstructure is comparable to as-built microstructures obtained by conventional SLM methods in as-built conditions, which have reported very high cooling rate ( $\sim 10^6$  K/s) and lowest build temperature [36]. Yang et al. observed a high density of dislocation tangles, twins and fine-scale  $\beta$ ; they argued that fine-scale  $\beta$  is unstable due to their XRD results did not show  $\beta$  peaks [18]. The authors did however observe a shift in (110) peaks compared to calculated lattice parameters, which they attributed to the increased solubility of V in  $\alpha'$ , which was not confirmed experimentally; other authors have argued that the peak shift is caused by solute redistribution [10]. Similar microstructures have been reported by several authors [36], however no elemental segregation at twins has been reported before.

On the other hand, the observed microstructure at 570°C is partially similar to microstructures obtained by SLM after heat treating the samples at medium to low temperatures. For instance, Xu et al. [8] used SEM to characterise the microstructure of SLM Ti-6Al-4V in as-built state and after applying different heat treatments. The Backscatter Electron images (BSE) of the as-built samples did not show evidence of forming nano-scale  $\beta$  at grain boundaries, however when post-LPBF tempering at 540 °C, isolated nano particles of  $\beta$  along the  $\alpha$  boundaries were observed. The authors also reported that the decomposition of martensite takes place at temperatures as low as 400 °C. No elemental segregation at dislocations was reported.

The observed microstructure at 770°C is similar to microstructures obtained by Electron Beam Melting (EBM), where the cooling rate is less severe ( $\sim 10^4$  K/s) and the local build temperature is

comparable [37]. For instance, Tan et al. [5] studied the transition of  $\beta$  to  $\alpha'$  and  $\alpha$  during EBM by means of Atom Probe and SEM. To do this they varied the thickness of the built samples to determine the variations in microstructure, thin samples were fully martensitic and thick samples contained primarily  $\alpha+\beta$ . Their Atom Probe results showed local elemental enrichment (V) at dislocations in martensitic samples (thin) but no segregation at twins was reported, whereas the composition in the thick samples corresponded to that at equilibrium in an  $\alpha+\beta$  microstructure. They argued that discrete  $\beta$  particles form initially along the  $\alpha'$  plate boundaries and grow subsequently, however they only referred to the low possibility of finding connecting  $\beta$  rods within the  $\alpha'$  plates.

In summary, the microstructures of titanium alloys are incredibly sensitive to thermal processing and thermal history. Parameters such as cooling rate, both above and below the  $\beta$  transus, are critical to the resultant microstructure, which is directly linked to the final strength and fatigue performance [32,38]. Extended time at temperature due to substrate heating as seen here will therefore act as pseudo ageing, comparable to standard processes. This has a significant effect on the local chemistry and diffusion and how this interacts with defects within the material, as well as microstructural evolution.

### 4.3 Phase kinetics and relation with martensite transformation parameters.

The phase transformation sequence in Ti-6Al-4V produced by SLM and EBM differs during the final stages but is similar during the initial stages of the thermal cycle [5,18], which can serve as baseline for analysing the transformation sequence in the present work. The sequence for SLM and EBM is as follows: during the first cycle  $\beta$  forms upon solidification which rapidly transforms into  $\alpha'$  due to the very high cooling rates; during subsequent cycles,  $\alpha'$  partially transforms back to  $\beta$  upon reheating, which then transforms again to  $\alpha'$  upon cooling, leading to primary and secondary  $\alpha'$ ; a small fraction of retained  $\beta$  remains during the build process and  $\alpha'$  eventually transforms to  $\alpha+\beta$  in EBM. In order to understand the differences in the primary phases observed at different preheating temperatures (**Table 3**), it is important to also identify the transformation kinetics of  $\beta$  to  $\alpha$  and  $\beta$  to  $\alpha'$  in Ti-6Al 4V. The martensite start,  $M_s$ , and finish,  $M_f$ , temperatures have been estimated as  $\sim 790^\circ\text{C}$  and  $\sim 710^\circ\text{C}$ , respectively [39], whereas the  $\alpha$  start, i.e.  $\beta$  transus, and finish are  $980^\circ\text{C}$  and  $\sim 570^\circ\text{C}$ , respectively.

At  $770^\circ\text{C}$ , the substrate is just below the  $M_s$  and above  $M_f$ , therefore much less  $\alpha'$  forms during the first and subsequent thermal cycles and the substrate spends a significantly longer time in the  $\alpha + \beta$  phase field, leading to more energy being supplied for diffusion. As  $\alpha$  is a more stable a preferable phase than  $\alpha'$ , and more prevalent at slower cooling rates, a lack of  $\alpha'$  is observed in this specimen. Possible slower cooling additionally means that as the material is cooled through the  $\beta$  transus, mass phase change occurs. This is evident in the tangled dislocations in **Figure 8** and the small  $\beta$  particles that are observed. Geometrically necessary dislocations are prevalent in these types of microstructures due to the misfit between the  $\alpha$  and  $\beta$  phases [21,40], where the  $\beta$  phase is much larger, resulting in both a strain and rotation to create a favourable low energy interface. Once the  $\beta$  phase has transformed upon cooling, these dislocations will still be present, and furthermore may explain the partitioning of  $\beta$  stabilisers to dislocations.

At  $570^\circ\text{C}$ , higher undercooling promotes significant  $\alpha'$  formation and, since the preheating is at  $\alpha$ , nucleation will also be thermodynamically favourable but after longer times; as the preheating temperature is below  $M_f$ ,  $\alpha$  will likely nucleate from the  $\alpha'$  by solute partitioning. However, at this temperature the energy for chemical diffusion is lower, providing a much slower growth velocity for the  $\alpha$  phase [41,42]. Nano  $\beta$  is observed at this substrate temperature and is less prevalent than at  $770^\circ\text{C}$ , however APT shows an increase of vanadium at the  $\alpha/\alpha'$  boundary which could indicate a much finer presence of  $\beta$  within the microstructure.

This analysis also indicates that for preheating temperatures below 570°C, e.g. at 100°C, the microstructures will be primarily martensitic with  $\alpha$  eventually forming and a small fraction of  $\beta$  might be possible if there is enough thermal energy for elemental diffusion;  $\alpha'$  will decompose above , as  $\alpha$  nucleation will be more prolific, therefore leading primarily to  $\alpha+\beta$ . Our analysis in **Table 3** is consistent with these conclusions.

As for other microstructural features, microtwinning in  $\alpha'$  is only observed when preheating at 100°C, whereas the IPF maps for 570°C and 770°C in **Figure 5** showed a somewhat resemblance of an initially twinned microstructure but it has evolved into lamellar  $\alpha+\beta$ . This indicates that in-situ recovery has taken place at higher preheating temperatures, however it was not possible to find information on the recovery kinetics of twinning in Ti-6Al-4V during high temperature annealing. Nonetheless, if the athermal transformation from  $\beta$  to  $\alpha'$  is rationalised as an introduction of shear deformation in the sample, we can qualitatively compare the behaviour of twinning observed in the present work with that for mechanical twinning in Ti-6Al-4V deformed at different temperatures. Mechanical twinning in Ti-6Al-4V typically occurs only when it is deformed at very high strain rates or very low temperatures [43]. Under such conditions, mechanical twinning has been reported to form up to a maximum deformation temperature of ~400°C-450°C. Hao et al [44] reported in the near- $\alpha$  alloy Ti-6Al-2Zr-1Mo-V wt% that twinning forms under tension at and below 400°C. Similarly, Zeng et al [45] reported in commercially pure Ti that twinning is suppressed at 650°C and Fitzner et al [46] reported that twinning forms at room temperature in near- $\alpha$  Ti-Al alloys with Al up to 12at%, whereas for higher Al contents it is suppressed due to the activation of basal slip. Therefore, since twinning impedes dislocation motion and potentially lowering material's ductility, if the preheating conditions are above 400°C-450°C the ductility can in principle increase via promoting twin recovery.

#### 4.4 Effect of Solute and Solute segregation in mechanical properties

Another important aspect to remark is the occurrence of solute segregation at crystal defects in all pre-heating conditions, even at temperatures as low as 100°C. Solute segregation at crystal defects in martensite has been reported for C diffusing to dislocations and twins in Fe [47]. More recently, Tan et al [5] reported similar solute behaviour in Ti-6Al-4V built by Electron Beam Melting. They observed that as  $\alpha'$  decomposes by higher local thermal exposure, vanadium and aluminium in  $\alpha'$  segregate and deplete at the  $\alpha/\beta$  forming interface, respectively. They also observed that the width of the  $\alpha/\beta$  interface widened with increasing the local build temperature and attributed the widening to an increase of strength; the latter was as the  $\alpha/\beta$  interface act as barriers against dislocation motion. In the present case, no such segregation and depletion was observed and it was not possible to determine whether a similar widening effect took place when changing the pre-heating temperature. This is probably because the effective built temperatures are much lower than the built temperature in EBM conditions. Nonetheless, to the authors knowledge, this is the first time that “selective” segregation phenomena at twins and V segregation at dislocations in LPBF Ti-6Al-4V is reported.

In order to rationalise the effect of solute segregation to crystal defects in the loss of ductility at different build temperatures, a model for the local concentration change at crystal defects is combined with an equation for the local change in the critical resolved shear stress by solid solution strengthening. The former is described by the equation:

$$\Delta c = c_0 \tanh\left(\frac{\Delta W}{2k_B T}\right) \left(1 - \exp\left(1 - 16 \cosh\left(\frac{\Delta W}{2k_B T}\right) \Gamma_0 t\right)\right),$$

where  $c_0$  is the nominal solute concentration,

$\Delta W$  is the average solute binding energy to a crystal defect,  $\Gamma_0 = v_0 \exp\left(-\frac{\Delta H}{k_B T}\right)$  is the solute transition rate with  $v_0 = 13.7 \times 10^{12} \text{s}^{-1}$  and  $\Delta H$  being the enthalpy of migration. The previous equation has been derived to describe solute segregation to dislocations in Al alloys and O segregation at twins in  $\alpha$ -Ti [48,49]. Since the equation does not make explicit reference to the

nature of the crystal defect, we assume in the present case that is for twins at 100 °C and for dislocations and grain boundaries at 570 °C and 770 °C. Parameters for O, Al and V in Ti were obtained from [49–51] and respectively are (consider diffusion along basal planes):  $\Delta W = 0.18$  eV, 0.1 eV, 0.07 eV and  $\Delta H = 1.496$  eV, 2.03 eV and 2.01 eV<sup>1</sup>. The associated solid solution strengthening term is calculated using the formula originally derived by Labusch [52]:  $\Delta\sigma_{ss} = \beta_{ss}\Delta c^{2/3}$ , where  $\beta_{ss}$  is a constant incorporating effects of local changes in modulus and lattice strain by solute atom in Ti.  $\beta_{ss} = 1813$  MPa and 127 MPa for Al and V in  $\alpha$ -Ti, respectively, were obtained in previous work [52], whereas  $\beta_{ss} = 9067$  MPa for O was obtained by fitting the equation to experimental data from [53].

**Table 4** shows the predicted values of  $\Delta c$  and  $\Delta\sigma_{ss}$  for the 3 build conditions after 1h. Nominal compositions for Al and V in  $\alpha$  were considered, i.e.  $c_0 = 10$  at% and 3.5 at%, respectively, whereas for O was assumed 0.7 at%, consistent with the O measured for 100 °C (in Table 2). Although no O segregation at dislocations was found in the sample analysed, its concentration is higher in  $\alpha'$ , which has a high dislocation density, and also O has a high diffusivity in  $\alpha$ , indicating that it will likely segregate at dislocations during mechanical loading; hence, we consider its possible effect on segregation at dislocations. Except for the 100 °C condition, the predicted values are of the same order of magnitude than those measured with the atom probe in **Figs. 10-12**. Very little segregation was predicted at 100 °C, whereas a local variation of  $\pm 4$  at% Al and  $\pm 1$  at% V segregation at twins was measured in **Figure 11**. At 570 °C, a local segregation of 5.9 at% and 1.56 at% in Al and V was predicted, whereas local variations of  $\sim 2$  at% in Al and V at  $\alpha/\alpha$  boundaries were measured in **Figure 10c**. Slightly lower segregation was predicted at 770 °C with 5 at% and 1.3 at% for Al and V, respectively, whereas  $\sim 3$  at% of V segregation at dislocations was measured in **Figure 12**, though no Al segregation at dislocations was detected; in this case, we can consider the segregation reaction as the change in Al content measured between  $\alpha'$  and  $\alpha$  (3.85 at%, **Table 2**). The discrepancy at 100 °C can be due to the inaccuracy in the used values for the models, as it was only tested for O in Ti [49]. The contribution to solid solution strengthening of O for the 570 °C and 770 °C conditions is predicted to be in the range of 275-300 MPa and 250-275 MPa, respectively, whereas very little strengthening from V was estimated. The results indicate that the local solid solution strengthening increment by the presence of O can be responsible for keeping the macroscopic strength nearly constant in spite of the microstructure is clearly coarsening with increasing preheating temperature. It is worth mentioning that although the contribution of V to solid solution strengthening in  $\alpha/\alpha'$  is small, its influence on mechanical properties is more significant via stabilising  $\beta$ . The results also indicate that, if Al segregation at twins for 100 °C is considered, a local increase in solid solution strengthening of  $\sim 200$  MPa takes place for this condition; this effect is not considered in 570 °C and 770 °C as no Al segregation at dislocations was detected. As for the implications in loss of ductility, Yan et al. have reported that drastic loss in ductility in C&W Ti-64 when O is above  $\sim 0.4$  wt%, although a similar trend for its AM counterpart was less clear. This is because of the different resulting microstructures;  $\alpha'$  had the lowest tolerance with only  $\sim 0.20$ - $0.25$  wt% of O before dramatic loss in elongation was reported, whereas  $\alpha + \beta$  had an O tolerance of up to 0.36 wt%. In the present case, 770 °C had the highest O content in  $\alpha'$  with 0.43 wt% (1.26 at%), whereas at 570 °C it was 0.25 wt%, indicating that O in the latter was at or just below the limit for rapid loss in ductility.

**Table 4.** Predicted local Al, V and O concentrations at crystal defects and their influence on local variations in solid solution strengthening.

<sup>1</sup> Values for Al and V were obtained from [50] and [51] respectively, by considering  $0.75Q$ , with  $Q$  being the activation energy for diffusion. This is roughly the ratio between the activation energy for O diffusion near a twin boundary in Ti [54].

Element	$\Delta c$ (at%)			$\Delta\sigma_{ss}$ (MPa)		
	100 °C	570 °C	770 °C	100 °C	570 °C	770 °C
Al	~0	5.96	5.05	~0	276.9	247.8
V	~0	1.56	1.298	~0	7.9	7
O	0.02	0.6	0.53	37.9	296.5	276.8

In conclusion, the role of solute segregation at crystal defects seems to have a dual effect: Al and O promote local solid solution strengthening which increases the local critical resolved shear stress for dislocation slip and maintains the high strength induced by the initial martensitic structure, but the excess of O at high temperatures surpasses the maximum threshold for O tolerance in  $\alpha'$  and rapidly lowers its ductility.

## Conclusions

Samples of Ti-6Al-4V were produced through LPBF on a heated substrate between 100-770°C. Increasing the temperature of the substrate from 100°C to 570°C improved the ductility during room temperature tensile tests, with 570°C being the ductility maximum. Further heating of the substrate during sample production up to 770°C reduced ductility to zero. Although the ductility changed significantly with processing conditions, the UTS at 100°C and 570°C was approximately constant (~1.2GPa) and it had the lowest value at 770°C, probably due to the alloy's brittle behaviour. Our analysis employed SEM, TEM and APT to study the complex variations in microstructure and solute behaviour to establish the specific mechanisms controlling the strength and ductility at different substrate temperatures. In summary:

- At 100°C, a heavily strained and twinned microstructure, primarily composed of  $\alpha+\alpha'$ , was observed and it was comparable to as-built microstructures obtained by conventional LPBF methods. The low ductility of this sample was attributed to the high density of microtwins and dislocations preventing any further plasticity and/or dislocation slip. At 570°C, twins are no longer present and instead nano-scale  $\beta$  precipitates are observed within  $\alpha'$  and  $\alpha$ , as well as dislocation networks. The lack of twins was attributed to this temperature being higher than the temperature for twin recovery in Ti-6Al-4V (~400°C-450°C). The microstructure at 570°C was partially similar to microstructures obtained by conventional LPBF after heat treating the samples at medium to low temperatures. At 770°C, there is substantially more  $\beta$ , very little  $\alpha'$  remains, and dislocation tangles form within the  $\alpha$  grain interiors. The observed microstructure at 770°C is similar to microstructures obtained by Electron Beam Melting, where the local build temperature is comparable and the cooling rates are less severe, leading to a mix of  $\alpha+\beta$  and small residual  $\alpha'$ .
- The dislocation networks observed in the 570°C sample may have formed by a sequence of interfacial dislocations generating at the  $\alpha'/\beta$  interface as  $\alpha'$  nucleates during rapid cooling. The substrate temperatures were high enough to promote dislocation recovery but grain-boundary  $\beta$  precipitates could have inhibited significant dislocation annihilation and local dislocation reconfiguration takes place instead. It was concluded that dislocation networks in the 570°C sample act as "soft barriers" for slip and help in increasing the ductility.
- The dislocation tangles observed at 770°C could have formed by a similar mechanism but the higher build temperature promotes extensive recovery and partial network dissolution. Evidence of this was that well-defined networks were still present in the vicinity of the  $\alpha/\beta$  interfaces, where grain-boundary  $\beta$  should limit the extent of dislocation recovery by maintaining the interfacial misfit. The lack of ductility at 770°C was attributed to local solute redistribution causing dislocation pinning and an increase of O content in this sample, particularly at  $\alpha'$  where a high dislocation density is present.

- Solute segregation at crystal defects was observed in all pre-heating conditions. Al and V segregation at microtwins was observed in the 100°C sample, with mutually exclusive Al- and V-rich regions forming in adjacent twins. This indicates that the shear strain induced by twinning induces a driving force high enough for solute partitioning and short range diffusion towards forming  $\alpha$  and  $\beta$  in the Al- and V-rich regions. To the authors knowledge, it is the first time such “selective” solute partitioning at twins is observed in Ti.
- V segregation at dislocations was observed in the 570°C and 770°C samples, consistent with the higher preheating temperatures. The observations are in agreement with previous reports in Ti-6Al-4V produced by Electron Beam Powder Fusion but, to the authors knowledge, this is the first work reporting solute segregation at dislocations in Ti-6Al-4V using Laser-based technologies.
- High O contents were measured in all samples. At 570°C and 770°C, Oxygen promotes an increase in the solid solution strengthening of ~375-300 MPa, potentially aiding in maintaining the strength high. This can be reflected in the macroscopic strength being nearly identical at 570°C and 100°C, in spite of the microstructure being coarse in the former. However, O contents at 770°C were just above the threshold for O embrittlement, therefore the sample showed a lack of ductility. At 100°C and 570°C, the O was measured to be below the critical threshold.
- Based on the complicated phase transformation sequences and microstructural variations analysed in this work, optimal in-situ heat treatments for improved microstructural control and mechanical properties should likely be in the temperature range of 450°C-570°C. This processing window results in a strong (~1.2GPa) and fine  $\alpha'+\alpha+\beta$  structure containing a high density of dislocation networks, acting as soft barriers for slip increasing the ductility. The relatively-high temperatures also promote short-range diffusion for solute segregation and localised solid solution strengthening for improved strength. This temperature range should produce samples below the critical Oxygen content for severe embrittlement, whilst the O adsorbed during the build process may promote additional solid solution strengthening, although the actual levels of O absorption are material, machine and process-specific.

## Acknowledgements

E.I. Galindo-Nava, S. Pedrazzini and T. B. Britton would all like to acknowledge the Royal Academy of Engineering for their research fellowships. E.I. Galindo-Nava performed this work under EPSRC grant EP/T008687/1. S. Pedrazzini performed part of this work under EPSRC grant EP/M005607/1 and under EPSRC fellowship EP/S0138881/1. Giorgio Divitini is gratefully acknowledged for his help with TEM. P. Bajaj acknowledges funding by the DFG under grant number JA2482/2-1. EPSRC Future Manufacturing Hub in Manufacture using Advanced Powder Processes (MAPP)(EP/P006566/1) is acknowledged for their support during this investigation. T. Dessolier and T. B. Britton acknowledge funding from the Shell-Imperial Advances Interfacial Materials Science (AIMS) Centre.

## References

- [1] R.R. Boyer, Titanium for aerospace: Rationale and applications, *Adv. Perform. Mater.* 2 (1995) 349–368. <https://doi.org/10.1007/BF00705316>.
- [2] R.R. Boyer, An overview on the use of titanium in the aerospace industry, 213 (1996) 103–114.
- [3] L.P. Borrego, J.A.M. Ferreira, J.D.M. Costa, C. Capela, J. De Jesus, A study of fatigue notch sensibility on titanium alloy TiAl6V4 parts A study of fatigue notch sensibility on titanium alloy TiAl6V4 parts manufactured by selective laser melting, *Procedia Struct. Integr.* 13 (2018) 1000–1005. <https://doi.org/10.1016/j.prostr.2018.12.186>.

- [4] K.S. Chan, M. Koike, R.L. Mason, T. Okabe, Fatigue life of titanium alloys fabricated by additive layer manufacturing techniques for dental implants, *Metall. Mater. Trans. A Phys. Metall. Mater. Sci.* 44 (2013) 1010–1022. <https://doi.org/10.1007/s11661-012-1470-4>.
- [5] X. Tan, Y. Kok, W.Q. Toh, Y.J. Tan, M. Descoins, D. Mangelinck, S.B. Tor, K.F. Leong, C.K. Chua, Revealing martensitic transformation and  $\alpha/\beta$  interface evolution in electron beam melting three-dimensional-printed Ti-6Al-4V, *Sci. Rep.* 6 (2016) 1–10. <https://doi.org/10.1038/srep26039>.
- [6] T. Vilaro, C. Colin, J.D. Bartout, As-Fabricated and Heat-Treated Microstructures of the Ti-6Al-4V Alloy Processed by Selective Laser Melting, (n.d.). <https://doi.org/10.1007/s11661-011-0731-y>.
- [7] B. Vrancken, L. Thijs, J. Kruth, J. Van Humbeeck, Heat treatment of Ti6Al4V produced by Selective Laser Melting : Microstructure and mechanical properties, *J. Alloys Compd.* 541 (2012) 177–185. <https://doi.org/10.1016/j.jallcom.2012.07.022>.
- [8] W. Xu, M. Brandt, S. Sun, J. Elambasseril, Q. Liu, K. Latham, K. Xia, M. Qian, Additive manufacturing of strong and ductile Ti – 6Al – 4V by selective laser melting via in situ martensite decomposition, *Acta Mater.* 85 (2015) 74–84. <https://doi.org/10.1016/j.actamat.2014.11.028>.
- [9] Y. Sakurai, K. Kakehi, Microstructure and Mechanical Properties of Ti –6Al –4V parts build by Selective Laser Melting, *J. Japan Inst. Met. Mater.* (2017) 120–126.
- [10] G. Li, J. Li, X. Tian, X. Cheng, B. He, H. Wang, Materials Science & Engineering A Microstructure and properties of a novel titanium alloy Ti-6Al-2V-1 . 5Mo-, *Mater. Sci. Eng. A.* 684 (2017) 233–238. <https://doi.org/10.1016/j.msea.2016.11.084>.
- [11] S. Leuders, S. Meiners, L. Wu, A. Taube, T. Tröster, T. Niendorf, Structural components manufactured by Selective Laser Melting and Investment Casting — Impact of the process route on the damage mechanism under cyclic loading, 248 (2017) 130–142. <https://doi.org/10.1016/j.jmatprotec.2017.04.026>.
- [12] S. Tammas-williams, P.J. Withers, I. Todd, P.B. Prangnell, Communication The Effectiveness of Hot Isostatic Pressing for Closing Porosity in Selective Electron Beam Melting, *Metall. Mater. Trans. A.* 47 (2016) 1939–1946. <https://doi.org/10.1007/s11661-016-3429-3>.
- [13] M. Benedetti, M. Cazzolli, V. Fontanari, M. Leoni, Fatigue limit of Ti6Al4V alloy produced by Selective Laser Sintering modeling high pressure turbine blade of an airplane gas turbine engine, *Procedia Struct. Integr.* 2 (2016) 3158–3167. <https://doi.org/10.1016/j.prostr.2016.06.394>.
- [14] H. Ali, L. Ma, H. Ghadbeigi, K. Mumtaz, In-situ residual stress reduction, martensitic decomposition and mechanical properties enhancement through high temperature powder bed pre-heating of Selective Laser Melted Ti6Al4V, *Mater. Sci. Eng. A.* 695 (2017) 211–220. <https://doi.org/10.1016/j.msea.2017.04.033>.
- [15] M. Ashby, The hardening of metals by non-deforming particles, *Z. Met.* 55 (1964) 5–17.
- [16] J. Yang, H. Yu, J. Yin, M. Gao, Z. Wang, X. Zeng, Formation and control of martensite in Ti-6Al-4V alloy produced by selective laser melting, *JMADE.* 108 (2016) 308–318. <https://doi.org/10.1016/j.matdes.2016.06.117>.
- [17] X. Tan, Y. Kok, Y. Jun, G. Vastola, Q. Xiang, G. Zhang, Y. Zhang, S. Tor, K. Fai, C. Kai, An experimental and simulation study on build thickness dependent microstructure for electron beam melted Ti e 6Al e 4V, *J. Alloys Compd.* 646 (2015) 303–309. <https://doi.org/10.1016/j.jallcom.2015.05.178>.

- [18] J. Haubrich, J. Gussone, P. Barriobero-vila, P. Kürnsteiner, D. Raabe, N. Schell, G. Requena, A.J. Eric, The role of lattice defects , element partitioning and intrinsic heat effects on the microstructure in selective laser melted Ti-6Al-4V, *Acta Mater.* 167 (2019) 136–148. <https://doi.org/10.1016/j.actamat.2019.01.039>.
- [19] H. Conrad, Effect of interstitial solutes on the strength and ductility of titanium, 26 (1981) 123–403.
- [20] P. Kontis, Z. Li, M. Segersäll, J.J. Moverare, R.C. Reed, D. Raabe, B. Gault, The Role of Oxidized Carbides on Thermal-Mechanical Performance of Polycrystalline Superalloys, *Metall. Mater. Trans. A.* 49 (2018) 4236–4245. <https://doi.org/10.1007/s11661-018-4709-x>.
- [21] A.K. Ackerman, V.A. Vorontsov, I. Bantounas, Y. Zheng, Y. Chang, T. McAuliffe, W.A. Clark, H.L. Fraser, B. Gault, D. Rugg, D. Dye, Interface characteristics in an  $\alpha+\beta$  titanium alloy, *Phys. Rev. Mater.* 4 (2020) 1–7. <https://doi.org/10.1103/PhysRevMaterials.4.013602>.
- [22] S. Liu, Y.C. Shin, Additive manufacturing of Ti6Al4V alloy: A review, *Mater. Des.* 164 (2019) 107552. <https://doi.org/https://doi.org/10.1016/j.matdes.2018.107552>.
- [23] M. Benedetti, E. Torresani, M. Leoni, V. Fontanari, M. Bandini, C. Pederzoli, C. Potrich, The effect of post-sintering treatments on the fatigue and biological behavior of Ti-6Al-4V ELI parts made by selective laser melting, *J. Mech. Behav. Biomed. Mater.* 71 (2017) 295–306. <https://doi.org/10.1016/J.JMBBM.2017.03.024>.
- [24] K. Mutombo, S. Charles, W. Stumpf, Phase transformation cycle  $\beta \rightarrow \alpha' + \alpha + \alpha'' \rightarrow \beta$  in Ti6Al4V alloy, *Mater. Sci. Forum.* 828–829 (2015) 232–238. <https://doi.org/10.4028/www.scientific.net/MSF.828-829.232>.
- [25] L.E. Murr, S.A. Quinones, S.M. Gaytan, M.I. Lopez, A. Rodela, E.Y. Martinez, D.H. Hernandez, E. Martinez, F. Medina, R.B. Wicker, Microstructure and mechanical behavior of Ti–6Al–4V produced by rapid-layer manufacturing, for biomedical applications, *J. Mech. Behav. Biomed. Mater.* 2 (2009) 20–32. <https://doi.org/10.1016/J.JMBBM.2008.05.004>.
- [26] J. He, C.H. Zenk, X. Zhou, S. Neumeier, D. Raabe, B. Gault, S.K. Makineni, On the atomic solute diffusional mechanisms during compressive creep deformation of a Co-Al-W-Ta single crystal superalloy, *Acta Mater.* 184 (2020) 86–99. <https://doi.org/10.1016/j.actamat.2019.11.035>.
- [27] S. Joseph, I. Bantounas, T.C. Lindley, D. Dye, Slip transfer and deformation structures resulting from the low cycle fatigue of near-alpha titanium alloy Ti-6242Si, *Int. J. Plast.* 100 (2018) 90–103. <https://doi.org/10.1016/j.ijplas.2017.09.012>.
- [28] E.I. Galindo-Nava, On the prediction of martensite formation in metals, *Scr. Mater.* 138 (2017) 6–11. <https://doi.org/https://doi.org/10.1016/j.scriptamat.2017.05.026>.
- [29] R.K. Rai, J.K. Sahu, S.K. Das, N. Paulose, D.C. Fernando, C. Srivastava, Cyclic plastic deformation behaviour of a directionally solidified nickel base superalloy at 850 °C: Damage micromechanisms, *Mater. Charact.* 141 (2018) 120–128. <https://doi.org/https://doi.org/10.1016/j.matchar.2018.04.039>.
- [30] C.J. Szczepanski, S.K. Jha, J.M. Larsen, J.W. Jones, The role of local microstructure on small fatigue crack propagation in an  $\alpha + \beta$  titanium alloy, Ti-6Al-2Sn-4Zr-6Mo, *Metall. Mater. Trans. A Phys. Metall. Mater. Sci.* 43 (2012) 4097–4112. <https://doi.org/10.1007/s11661-012-1228-z>.
- [31] F. Bridier, P. Villechaise, J. Mendez, Slip and fatigue crack formation processes in an  $\alpha/\beta$  titanium alloy in relation to crystallographic texture on different scales, *Acta Mater.* 56 (2008) 3951–3962. <https://doi.org/10.1016/j.actamat.2008.04.036>.
- [32] D.P. Satko, J.B. Shaffer, J.S. Tiley, S.L. Semiatin, A.L. Pilchak, S.R. Kalidindi, Y. Kosaka,

- M.G. Glavicic, A.A. Salem, Effect of microstructure on oxygen rich layer evolution and its impact on fatigue life during high-temperature application of  $\alpha/\beta$  titanium, *Acta Mater.* 107 (2016) 377–389. <https://doi.org/10.1016/j.actamat.2016.01.058>.
- [33] H. Conrad, Effect of interstitial solutes on the strength and ductility of titanium, *Prog. Mater. Sci.* 26 (1981) 123–403. [https://doi.org/10.1016/0079-6425\(81\)90001-3](https://doi.org/10.1016/0079-6425(81)90001-3).
- [34] M. Yan, W. Xu, M.S. Dargusch, H.P. Tang, M. Brandt, M. Qian, Review of effect of oxygen on room temperature ductility of titanium and titanium alloys, *Powder Metall.* 57 (2014) 251–257. <https://doi.org/10.1179/1743290114Y.0000000108>.
- [35] D. Banerjee, J.C. Williams, Perspectives on titanium science and technology, *Acta Mater.* 61 (2013) 844–879. <https://doi.org/10.1016/j.actamat.2012.10.043>.
- [36] S. Gorsse, C. Hutchinson, M. Gouné, R. Banerjee, Additive manufacturing of metals: a brief review of the characteristic microstructures and properties of steels, Ti-6Al-4V and high-entropy alloys, *Sci. Technol. Adv. Mater.* 18 (2017) 584–610. <https://doi.org/10.1080/14686996.2017.1361305>.
- [37] C. Körner, Additive manufacturing of metallic components by selective electron beam melting — a review, *Int. Mater. Rev.* 61 (2016) 361–377. <https://doi.org/10.1080/09506608.2016.1176289>.
- [38] G. Lütjering, Influence of processing on microstructure and mechanical properties of ( $\alpha+\beta$ ) titanium alloys, *Mater. Sci. Eng. A.* 243 (1998) 32–45. [https://doi.org/10.1016/S0921-5093\(97\)00778-8](https://doi.org/10.1016/S0921-5093(97)00778-8).
- [39] R. Dabrowski, The kinetics of phase transformations during continuous cooling of the Ti6Al4V alloy from the single-phase  $\beta$  range, *Arch. Metall. Mater.* 56 (2011) 703–707.
- [40] R.C. Pond, S. Celotto, J.P. Hirth, A comparison of the phenomenological theory of martensitic transformations with a model based on interfacial defects, *Acta Mater.* 51 (2003) 5385–5398. [https://doi.org/10.1016/S1359-6454\(03\)00395-1](https://doi.org/10.1016/S1359-6454(03)00395-1).
- [41] A.K. Ackerman, A.J. Knowles, H.M. Gardner, A.A.N. Németh, I. Bantounas, A. Radecka, M.P. Moody, P.A.J. Bagot, R.C. Reed, D. Rugg, D. Dye, The Kinetics of Primary Alpha Plate Growth in Titanium Alloys, *Metall. Mater. Trans. A Phys. Metall. Mater. Sci.* 51 (2020) 131–141. <https://doi.org/10.1007/s11661-019-05472-x>.
- [42] S. Mironov, M. Murzinova, S. Zhrebtsov, G.A. Salishchev, S.L. Semiatin, Microstructure evolution during warm working of Ti–6Al–4V with a colony- $\alpha$  microstructure, *Acta Mater.* 57 (2009) 2470–2481. <https://doi.org/10.1016/j.actamat.2009.02.016>.
- [43] D.G.L. Prakash, R. Ding, R.J. Moat, I. Jones, P.J. Withers, J.Q. da Fonseca, M. Preuss, Deformation twinning in Ti-6Al-4V during low strain rate deformation to moderate strains at room temperature, *Mater. Sci. Eng. A.* 527 (2010) 5734–5744. <https://doi.org/https://doi.org/10.1016/j.msea.2010.05.039>.
- [44] F. Hao, J. Xiao, Y. Feng, Y. Wang, J. Ju, Y. Du, K. Wang, L. Xue, Z. Nie, C. Tan, Tensile deformation behavior of a near- $\alpha$  titanium alloy Ti-6Al-2Zr-1Mo-1V under a wide temperature range, *J. Mater. Res. Technol.* 9 (2020) 2818–2831. <https://doi.org/https://doi.org/10.1016/j.jmrt.2020.01.016>.
- [45] Z. Zeng, Y. Zhang, S. Jonsson, Microstructure and texture evolution of commercial pure titanium deformed at elevated temperatures, *Mater. Sci. Eng. A.* 513–514 (2009) 83–90. <https://doi.org/https://doi.org/10.1016/j.msea.2009.01.065>.
- [46] A. Fitzner, D.G.L. Prakash, J.Q. da Fonseca, M. Thomas, S.-Y. Zhang, J. Kelleher, P. Manuel, M. Preuss, The effect of aluminium on twinning in binary alpha-titanium, *Acta Mater.* 103 (2016) 341–351. <https://doi.org/https://doi.org/10.1016/j.actamat.2015.09.048>.

- [47] W. Song, C. Drouven, E. Galindo-Nava, Carbon redistribution in martensite in high-C steel: Atomic-scale characterization and modelling, *Metals (Basel)*. 8 (2018) 1–12. <https://doi.org/10.3390/met8080577>.
- [48] W.A. Curtin, D.L. Olmsted, L.G. Hector, A predictive mechanism for dynamic strain ageing in aluminium–magnesium alloys, *Nat. Mater.* 5 (2006) 875–880. <https://doi.org/10.1038/nmat1765>.
- [49] M.S. Hooshmand, M. Ghazisaeidi, Solute/twin boundary interaction as a new atomic-scale mechanism for dynamic strain aging, *Acta Mater.* 188 (2020) 711–719. <https://doi.org/https://doi.org/10.1016/j.actamat.2020.01.066>.
- [50] L. Scotti, A. Mottura, Diffusion anisotropy of poor metal solute atoms in hcp-Ti, *J. Chem. Phys.* 142 (2015) 204308. <https://doi.org/10.1063/1.4921780>.
- [51] W.W. Xu, S.L. Shang, B.C. Zhou, Y. Wang, L.J. Chen, C.P. Wang, X.J. Liu, Z.K. Liu, A first-principles study of the diffusion coefficients of alloying elements in dilute  $\alpha$ -Ti alloys, *Phys. Chem. Chem. Phys.* 18 (2016) 16870–16881. <https://doi.org/10.1039/C6CP01899H>.
- [52] E.I. Galindo-Nava, Y.J. Jing, J. Jiang, Predicting the hardness and solute distribution during brazing of Ti-6Al-4V with TiZrCuNi filler metals, *Mater. Sci. Eng. A*. 712 (2018) 122–126. <https://doi.org/https://doi.org/10.1016/j.msea.2017.11.087>.
- [53] S. Bin, L.I. Shufeng, I. Hisashi, J. Umeda, K. Katsuyoshi, Oxygen Solid Solution Strengthened Pure Titanium Powder Materials †, *Trans. JWRI*. 41 (2012) 59–64. <http://www.jwri.osaka-u.ac.jp/publication/trans-jwri/pdf/411-11.pdf>.
- [54] M.S. Hooshmand, C. Niu, D.R. Trinkle, M. Ghazisaeidi, First-principles prediction of oxygen diffusivity near the  $(101\bar{2})$  twin boundary in titanium, *Acta Mater.* 156 (2018) 11–19. <https://doi.org/https://doi.org/10.1016/j.actamat.2018.05.076>.